

Elastic properties and hardness values of  $V_2AlC$  and  $Cr_2AlC$  single crystalsHussein O. Badr<sup>1</sup>, Aurélie Champagne<sup>2</sup>, Thierry Ouisse<sup>3</sup>, Jean-Christophe Charlier<sup>2</sup>, and Michel W. Barsoum<sup>1,\*</sup><sup>1</sup>Department of Materials Science and Engineering, Drexel University, Philadelphia, Pennsylvania 19104, USA<sup>2</sup>Institute of Condensed Matter and Nanosciences, Université catholique de Louvain, 1348 Louvain-la-Neuve, Belgium<sup>3</sup>Université Grenoble Alpes, CNRS, LMGP, Grenoble INP, 38000 Grenoble, France

(Received 26 May 2020; revised 10 July 2020; accepted 29 July 2020; published 26 August 2020)

Herein we report on a subset of the elastic constants,  $c_{ij}$ , and hardness values of  $V_2AlC$  and  $Cr_2AlC$  single crystals by means of microindentation/nanoindentation techniques. Density functional theory (DFT) is also used to calculate the elastic constants. The  $c_{33}$  and  $c_{11}$  values determined using a Berkovich tip and those calculated by DFT are all found to fall in the relatively narrow range of 320–350 GPa. These results confirm once again that many of MAX phases are relatively elastically isotropic, especially when compared to many other known layered solids such as graphite and mica. Similarly, the hardness values, obtained using Vickers, Berkovich, and a 5  $\mu\text{m}$  spherical tip on the two orthogonal  $Cr_2AlC$  surfaces, are quite comparable and average  $9.0 \pm 1$  GPa. In all cases, the hardness values are at most 20% higher when the basal planes are loaded along [0001] than when they are loaded edge-on. The  $Cr_2AlC$  surfaces record an average microyielding stress of  $2.7 \pm 0.3$  GPa, while the less defective  $V_2AlC$  crystals linearly sustain stresses of the order of 20 GPa, after which, in approximately 60% of the cases, pop-ins, some of which are substantial, are recorded. Postindentation scanning electron microscope micrographs clearly evidence the plastic anisotropy of these crystals. Large pileups near the indent edges and delamination cracks after loading along the [0001] and [10 $\bar{1}$ 0] directions, respectively, are consistent with deformation by ripplocations and ripplocation boundaries, as are the fully and spontaneously recoverable hysteresis stress-strain loops.

DOI: [10.1103/PhysRevMaterials.4.083605](https://doi.org/10.1103/PhysRevMaterials.4.083605)

## I. INTRODUCTION

Layered solids/composites, defined herein as systems in which the deformation, at least initially, is confined to two dimensions, are ubiquitous in nature. Such systems range over ten orders of magnitude or more in scale: from subnanometer graphene layers to wood, laminated composites, and paperboard at the centimeter scale to geologic formations in the kilometer range. One important commonality between these layered systems, be they wood, laminated composites, decks of cards, etc., or crystalline layered solids such as graphite [1], mica [2], and the MAX phases [3,4], is the formation of kink bands when the basal planes are loaded edge-on in compression.

The  $M_{n+1}AX_n$  (MAX) phases are layered, hexagonal (space group  $P6_3/mmc$ ), early transition metal carbides and nitrides, where  $n = 1, 2, 3,$  or  $4$ ,  $M$  is an early transition metal,  $A$  is an A-group element (mostly groups 13 and 14), and  $X$  is C, N, and/or B. In these phases,  $MX$  carbide/nitride layers are interleaved with pure “A” layers, which is why they are sometimes referred to as thermodynamically stable nanolaminates [5]. Currently, more than 150 MAX phases are known to exist [3]. As a class, the MAX phases, in general, are machinable, good thermal and electrical conductors, damage tolerant, and thermal shock resistant. Some of them, such as  $Ti_2AlC$ , are also stiff, oxidation resistant, and relatively light (approximately 4–5  $\text{g cm}^{-3}$ ) [6], with relatively low coefficients of thermal expansions [3,5]. More than two

decades ago,  $Ti_3SiC_2$ , the first member of the MAX family, was successfully synthesized in fully dense polycrystalline form by Barsoum and El-Raghy [7]. Since then, there have been numerous studies on their distinctive properties [4].

Characterizing the elastic and mechanical properties of solids and their anisotropies is important from both technological and scientific points of view. Despite the fact that the bonding in the MAX phases is a combination of metallic/covalent and the density of states at the Fermi level is substantial [5], when indented the MAX phases do *not* result in a metallurgical indentation [8]. Instead, they deform like much more brittle layered solids such as mica and graphite [8]. When indented normal to the basal planes, large pileups around the indenter are typically formed [8]. When the basal planes are indented edge-on, on the other hand, delamination cracks appear [8]. These characteristics, observed herein as well, stem from two factors. The first is that nonbasal dislocations have never been implicated in the deformation of these phases. This stems from the fact that their  $c/a$  ratios range from 4 to 7, which in turn renders the energy cost of nonbasal dislocations prohibitively expensive. The second factor is that the main deformation micromechanism is not basal dislocations, as has long been assumed, but rather ripplocations [8]. We have recently shown in a number of papers that atomic planes buckle like any other layered systems, whether they are decks of cards, thin steel sheets, or geological formations [8–10].

Depending on the elastic anisotropy of the layered system, the buckling can be localized or delocalized [11]. The latter is the preferred mode when elastic anisotropy is high, in solids such as graphite and mica or layers of paper, steel sheets,

\*Corresponding author: barsoumw@drexel.edu

playing cards, etc. [9]. In this case, at a critical stress, the system buckles into standing waves whose wavelength depends on the flexural stiffness and the thickness and number of individual sheets or atomic layers [9]. The crests of these standing waves define ripplication boundaries (RBs), which are fully or near fully reversible/recoverable [8–10]. The driving force for the reversibility is the elastic energy stored in the curvatures of the RBs, as well as the elastic energy in the material surrounding the RBs. If the applied load is too high, the RBs naturally convert to the ubiquitous kink boundaries (KBs), which cease to be reversible.

When the elastic properties are more isotropic, like in the MAX phases, the systems tend to buckle locally, resulting in either the aforementioned delamination cracks or large pileups at the edges of the indents [8]. Interestingly, in systems for which  $\langle c + a \rangle$  dislocations are possible, one obtains a metallurgical indentation, where the pileup is small and cracks are not observed [8]. In other words, delamination cracks or large pileups are the unmistakable signatures of deformation by ripplications for the simple reason that they are not possible in a basal dislocation framework.

As just noted, when layers are loaded edge-on in compression, at some critical load, they will form KBs. However, we have shown that before KBs form, there is a kinking nonlinear elastic regime characterized by fully, or near fully, recoverable stress-strain loops upon load cycling [10]. The friction between the layers can result in substantial energy dissipation during each cycle. The aforementioned RBs are responsible for this reversible response.

We have also shown over the years that repeat nanoindentation (NI) in the same location, especially with spherical tips, is quite a powerful method to probe the fundamental mechanics of how crystals, especially layered ones, deform [10]. The power of this approach is demonstrated herein as well. Further, while it is not possible to convert Berkovich load-displacement curves to stress-strain ones, it is possible to do so with spherical indenters. There have been a number of techniques to carry out this transformation; herein we use one we developed and are familiar with [12]. In brief, the elastic constants are extracted from stiffness  $S$  vs contact radii  $a$  curves on single crystals (see the Appendix and Fig. 7 [13,14]).

The purpose of this work is to report on the  $c_{33}$  and  $c_{11}$  values, as determined by NI, viz.,  $c_{33}^{\text{NI}}$  of  $\text{V}_2\text{AlC}$  and  $\text{Cr}_2\text{AlC}$  single crystals and  $c_{11}^{\text{NI}}$  of the latter, and compare these results with density functional theory (DFT) values. The elastic constants were determined using both a Berkovich and a  $5\ \mu\text{m}$ -radius,  $R$ , diamond tip. We also measured the Vickers microhardness values of the (0001) planes of  $\text{V}_2\text{AlC}$  and  $\text{Cr}_2\text{AlC}$  single crystals. These microhardness values were then compared to those obtained with the  $5\ \mu\text{m}$ -radius tip and the Berkovich indenter. When the latter was used, the Young's moduli and hardness values were calculated using the Oliver-Pharr method [15].

## II. EXPERIMENTAL DETAILS

### Material processing and characterization

The  $\text{V}_2\text{AlC}$  and  $\text{Cr}_2\text{AlC}$  single crystals were grown by a flux growth method [16,17]. Typical slow-cooling ramps

extended from  $1650\ ^\circ\text{C}$  to  $1100\ ^\circ\text{C}$  for  $\text{Cr}_2\text{AlC}$  and from  $1700\ ^\circ\text{C}$  to  $1200\ ^\circ\text{C}$  for  $\text{V}_2\text{AlC}$ . Growth takes place in alumina crucibles, and C incorporation is controlled by dipping a predetermined height of a rotating graphite rod in the solution at the highest temperature for 0.5 or 2 h for  $\text{Cr}_2\text{AlC}$  and  $\text{V}_2\text{AlC}$ , respectively. After the high-temperature step, aimed at dissolving all elements, the temperature is slowly decreased (over days) in order to enhance Ostwald ripening and decrease the number of small crystals in the solution. In the case of  $\text{V}_2\text{AlC}$ , growth is stopped at a temperature high enough so as to avoid an unwanted peritectic transformation of the grown crystals [17]. Crystals are extracted from the flux by Hydrochloric acid etching. The high-temperature solution growth parameters and the choice of the appropriate liquid composition are thoroughly described in Refs. [16,17]. Their single-crystal character is routinely assessed by measuring Laue x-ray-diffraction patterns measured in transmission.

The samples thicknesses were 53 and  $580\ \mu\text{m}$  for the  $\text{V}_2\text{AlC}$  and  $\text{Cr}_2\text{AlC}$  crystals, respectively. The  $\text{Cr}_2\text{AlC}$  single crystals were either mounted face-on on aluminum pucks, using a glue (Crystalbond, Ted Pella, Inc., Redding, CA), or embedded edge-on in epoxy (VersoCit-2, Struers Inc., Cleveland, OH). The same procedure was used for the  $\text{V}_2\text{AlC}$  crystal, except these samples were too thin for us to measure their edge-on properties. All samples were then polished to a mirror finish before the NI tests and Vickers hardness measurements were carried out.

The NI experiments were conducted at room temperature with a nanoindenter (XP system, MTS Corp., Oak Ridge, TN) equipped with a continuous stiffness measurement attachment. A hemispherical diamond tip with a radius  $R$  of  $5\ \mu\text{m}$  was used in addition to a Berkovich tip. The two tips were calibrated on a standard amorphous silica calibration sample before all tests. The same parameters were used for all of the NI tests, viz.,  $0.05\ \text{s}^{-1}$  strain rate,  $2\ \text{nm/s}$  unloading rate,  $2\ \text{nm}$  harmonic displacement target, a frequency of 45 Hz, and a maximum allowable drift rate of  $0.05\ \text{nm/s}$ .

Typically, the values of the load  $P$  and total displacement into the surface  $h_t$  were collected. Concomitantly, the harmonic contact stiffness  $S$  values were also recorded. In a typical NI test, the tip was loaded normal, or parallel, to the basal planes, in a load control mode, up to a given maximum load, held at the maximum load, and then fully retracted (Fig. 1). Multiple locations were indented and their results were averaged.

In this work, the elastic constants, as determined from NI,  $c_{33}^{\text{NI}}$  and  $c_{11}^{\text{NI}}$ , were calculated from the slope of the  $S$  vs  $a$  curves [Figs. 2(a) and 2(b)] obtained from the Berkovich and spherical tips. The results for both tips are listed in Table I. For the  $5\ \mu\text{m}$  spherical tip, the slope was calculated up to a maximum  $R \approx 1600\ \text{nm}$ . Beyond this value, the calculated values were slightly lower and thus no longer valid. Moreover, for the spherical tip, stress-strain curves were first determined and then the slopes of the linear elastic regime were calculated. These slopes represent the reduced moduli  $E$ . Equations (A4) and (A5) were then used to obtain the elastic constants.

In another set of experiments, with a  $5\ \mu\text{m}$  spherical tip, the load was initially applied, on a selected location, to the maximum load, retracted gradually to  $1\ \text{mN}$ , and then reloaded to the predetermined maximum load. These load-displacement

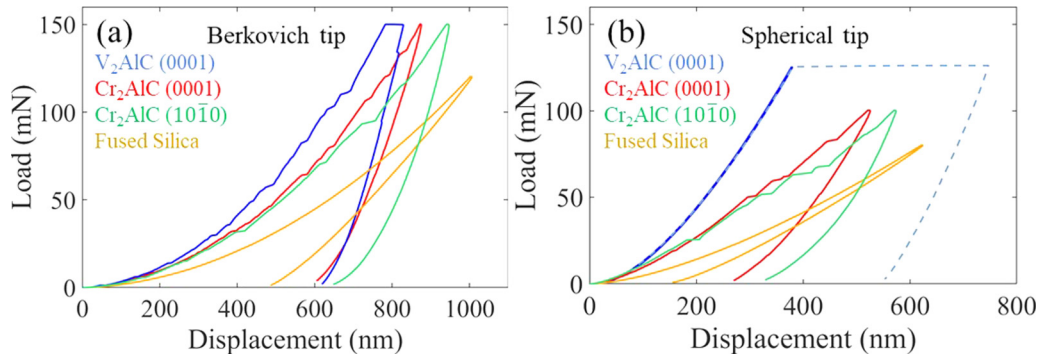


FIG. 1. Load vs displacement curves for the  $V_2AlC$  and  $Cr_2AlC$  (0001) and  $Cr_2AlC$  ( $10\bar{1}0$ ) surfaces and fused silica obtained when using (a) a Berkovich and (b) a  $5\ \mu m$ -radius spherical indenter.

data (not shown) were converted into NI stress  $\sigma_{NI}$  vs  $a/R$  plots (see Fig. 3) using procedures described previously [12] and summarized in the Appendix. Typically, the indenter is loaded to a maximum load, unloaded, and reloaded in the same location ten or so times.

Turning to the hardness measurements, NI hardness values were calculated with a Berkovich indenter using Oliver and Pharr's method [15]. Hardness vs indentation depth plots (shown in Fig. 4) were also generated for the  $5\ \mu m$  spherical tip, using an approach that was previously reported [14]. At 0.49 N, the maximum indentation force was kept relatively low to match the thinness of the samples used herein.

Vickers microhardness measurements were also performed on each crystal orientation when possible. The average lengths of the two orthogonal diagonals were determined from

scanning electron microscope, SEM (XL30, FEI Corporation, Hillsboro, OR) micrographs and converted to hardness values. Both sets of results are listed in Table II.

### III. COMPUTATIONAL DETAILS

The elastic constants of the  $V_2AlC$  and  $Cr_2AlC$  phases were computed *ab initio* using DFT [19,20] as implemented in the Vienna *ab initio* simulation package (VASP) [21–23]. The exchange-correlation functional was approximated using the generalized-gradient approximation as proposed by the Perdew-Burke-Ernzerhof (PBE) scheme [24]. Projector augmented wave pseudopotentials were used [25,26]. Configurations of  $C\ 2s^22p^2$ ,  $Al\ 3s^23p^1$ ,  $Cr\ 3d^54s^1$ , and  $V\ 3d^44s^1$  were treated as valence electrons. A plane-wave kinetic energy

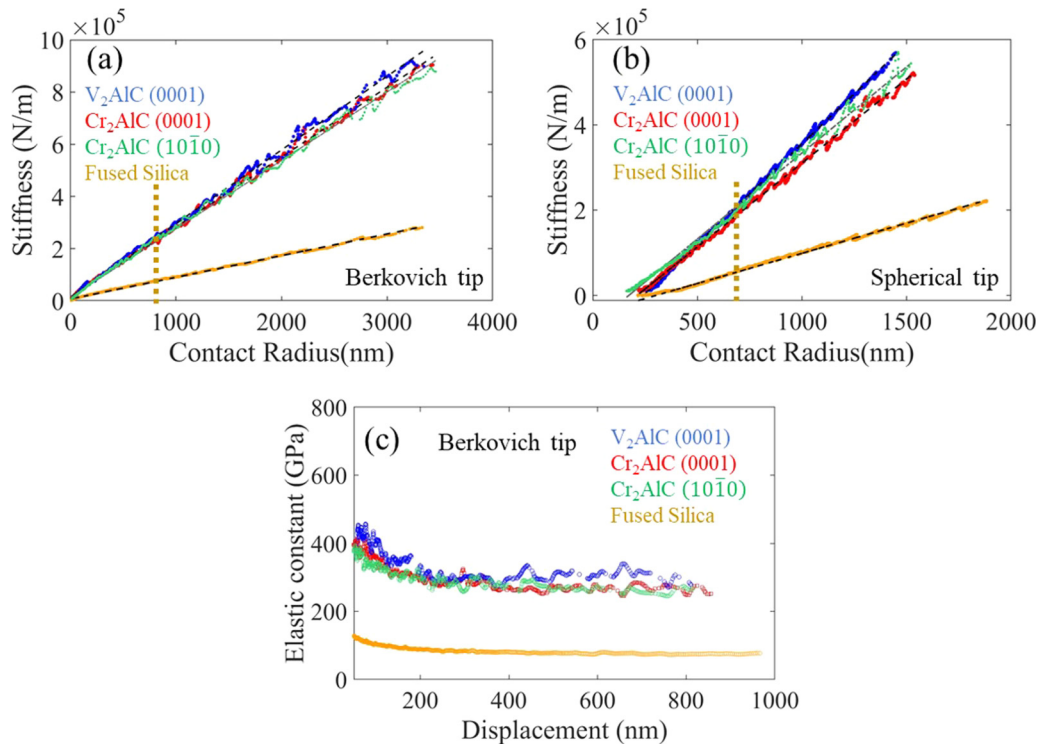


FIG. 2. Stiffness vs contact radii for  $V_2AlC$  and  $Cr_2AlC$  (0001) and  $Cr_2AlC$  ( $10\bar{1}0$ ) and fused silica surfaces obtained using (a) a Berkovich, and (b) a  $5\ \mu m$ -radius spherical indenter. (c) Dependence of elastic constants on total indentation depths of a Berkovich diamond tip for  $V_2AlC$  and  $Cr_2AlC$  (0001),  $Cr_2AlC$  ( $10\bar{1}0$ ), and fused silica surfaces.

TABLE I. Summary of elastic constant and modulus values in GPa obtained herein and in previous work. Numbers in parentheses denote the total number of indents performed to obtain the average and standard deviations listed.

Elastic constants/Moduli	Method/Tip	V <sub>2</sub> AlC (GPa)	Cr <sub>2</sub> AlC (GPa)
This Work			
c <sub>11</sub>	Berkovich		317 ± 10 (28)
c <sub>33</sub>	Berkovich	342 ± 17 (19)	320 ± 9 (18)
c <sub>11</sub>	DFT	328 <sup>a</sup>	347 <sup>a</sup>
c <sub>33</sub>	DFT	320 <sup>a</sup>	332 <sup>a</sup>
E <sub>H</sub>	DFT	314 ± 2	322 ± 11
Previous Work			
E	Berkovich	322 ± 45 [32]	298 ± 21 [33]
	Ultrasonic	283 [34]	285 [34]
	Ultrasonic	277 [35]	245 [35]
	DFT	306; 308; 319 [36],	358; 347; 332 [36]
	DFT	308 [37]	358 [37]
	DFT		316 [38]
c <sub>33</sub>	DFT		333 [38]
c <sub>33</sub>	DFT	319, 328, 314 [36]	369; 382; 382 [36]
c <sub>11</sub>	DFT	339, 338, 346 [36]	365; 396; 384 [36]
c <sub>11</sub>	DFT		345 [38]

<sup>a</sup>See Table III.

cutoff of 520 eV was used and the first Brillouin zone was sampled with a  $12 \times 12 \times 4$  Monkhorst-Pack  $k$ -point grid [27]. A Gaussian smearing of 0.2 eV was used to accelerate the convergence. For both systems, but especially for Cr<sub>2</sub>AlC [28], lattice parameter optimization led to an underestimation of the real values and consequently to an overestimation of the bonding strengths and elastic constants. The lattice parameters were therefore fixed to the experimental values reported in [29] and measured from our samples, and the atomic positions were optimized until the largest force was smaller than 0.1 meV/Å. Both sets of results are listed in Table III.

Additionally, the single-crystal elastic tensor of each system was determined by applying a set of homogeneous finite deformations and calculating the associated resulting stress, as implemented in the VASP code [21–23]. For hexagonal symmetry, there are five independent elastic constants  $c_{ij}$ , viz.,  $c_{11}$ ,  $c_{12}$ ,  $c_{13}$ ,  $c_{33}$ , and  $c_{44}$  [30]. Table III lists the  $c_{ij}$  values computed at zero pressure and absolute temperature for both V<sub>2</sub>AlC and Cr<sub>2</sub>AlC. In both cases,  $c_{11} > c_{33}$ .

For hexagonal crystals, the Voigt bulk  $B_V$  and shear  $G_V$  moduli (upper bound) can be obtained, respectively, assuming [30]

$$B_V = \frac{1}{9}[2(c_{11} + c_{12}) + 4c_{13} + c_{33}],$$

$$G_V = \frac{1}{15}(2c_{11} + c_{33} - c_{12} - 2c_{13}) + \frac{1}{5}[2c_{44} + \frac{1}{2}(c_{11} - c_{12})].$$

The Reuss bulk  $B_R$  and shear moduli  $G_R$  (lower bound) are given, respectively, by [30]

$$B_R = \frac{(c_{11} + c_{12})c_{33} - 2c_{13}^2}{c_{11} + c_{12} + 2c_{44} - 4c_{13}},$$

$$G_R = \frac{5}{2} \left( \frac{c^2 c_{44} c_{66}}{3B_V c_{44} c_{66} + c^2(c_{44} + c_{66})} \right),$$

where  $c_{66}$  is obtained assuming  $\frac{1}{2}(c_{11} - c_{12})$  and  $c = (c_{11} + c_{12})c_{33} - 2c_{13}^2$ . The arithmetic averages of Voigt and Reuss moduli are known as the Hill moduli, given by [31]

$$B_H = \frac{B_V + B_R}{2}, \quad G_H = \frac{G_V + G_R}{2}.$$

Using the calculated values of  $B_H$  and  $G_H$ , the average Young's modulus  $E$  and the Poisson ratio  $\nu$  can be obtained, respectively, assuming [31]

$$E_H = \frac{9B_H G_H}{3B_H + G_H}, \quad \nu = \frac{3B_H - 2G_H}{2(3B_H + G_H)}.$$

Starting with the DFT calculated  $c_{ij}$  values, the values of  $B_H$ , etc., were calculated and the results are listed in Table III together with those previously reported.

## IV. RESULTS

### A. Load-displacement curves

Figure 1(a) shows typical NI load-displacement curves obtained using a Berkovich tip, loaded to a maximum load of 150 mN, for the V<sub>2</sub>AlC (0001), Cr<sub>2</sub>AlC (0001), and Cr<sub>2</sub>AlC (10 $\bar{1}$ 0) surfaces. For the fused silica (SiO<sub>2</sub>) surface the maximum force was 120 mN. The corresponding curves for the spherical indenter are shown in Fig. 1(b). The SiO<sub>2</sub> surface was used for calibrating the indenter (discussed below). From these results the following points are salient: A cascade of small, discontinuous, and uneven pop-ins is observed in both the Berkovich [Fig. 1(a)] and spherical tips for the Cr<sub>2</sub>AlC (0001) and (10 $\bar{1}$ 0) surfaces [Fig. 1(b)]. The same behavior was observed for the (0001) V<sub>2</sub>AlC surface [Fig. 1(a)]. Notably, but not surprisingly, these are totally absent for the SiO<sub>2</sub> results. In some locations for the (0001) V<sub>2</sub>AlC surface massive pop-ins were observed [dotted line in Fig. 1(b)].

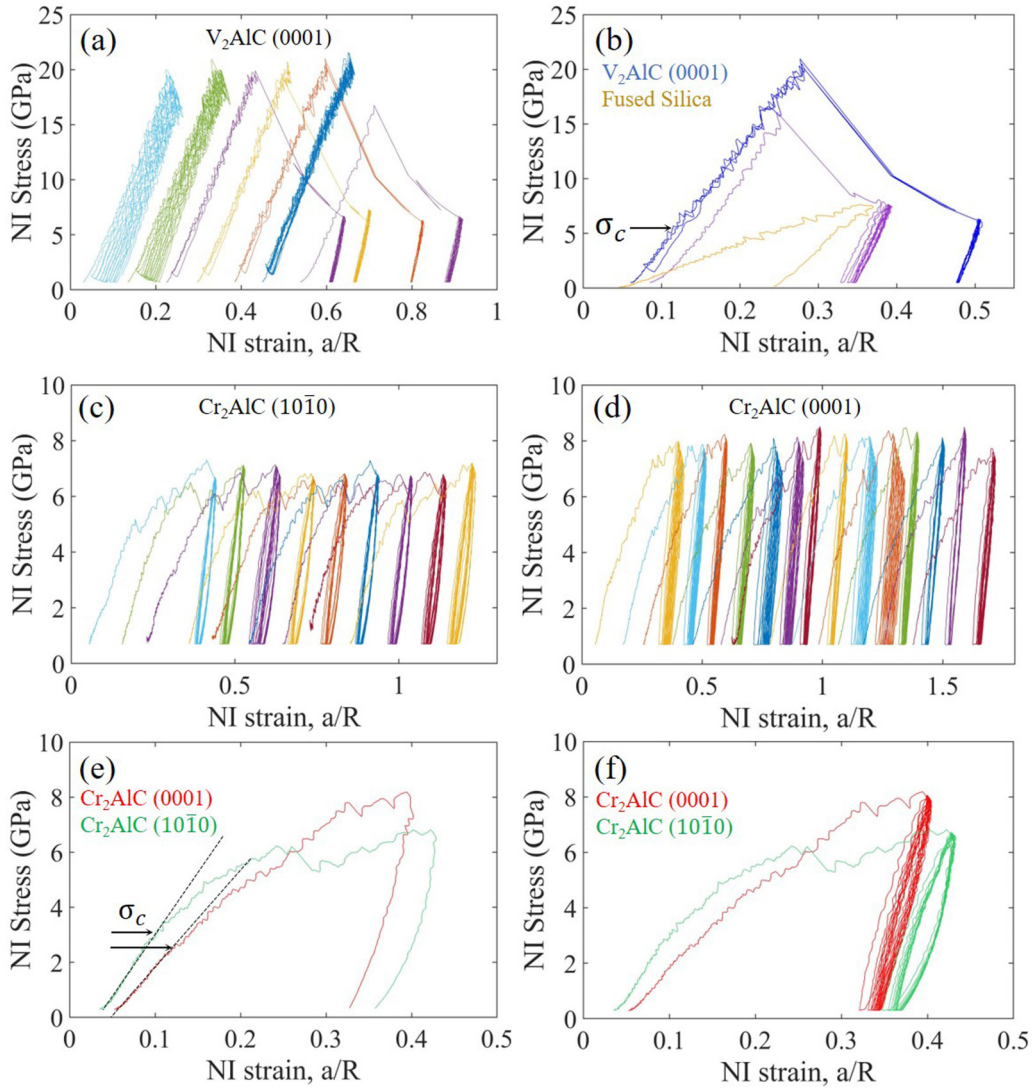


FIG. 3. Plot of NI stress vs  $a/R$  curves for (a) the  $V_2AlC$  (0001) surface and (b) same as (a) but focusing on two locations where two quite different pop-ins were recorded. Results for silica are plotted for comparison. Also shown are plots for the (c)  $(10\bar{1}0)$  and (d) (0001)  $Cr_2AlC$  surfaces, (e) two  $Cr_2AlC$  surfaces during first cycle, and (f) same as (e) but showing all 12 cycles. In (a), (c), and (d) the curves are shifted horizontally for the sake of clarity.

These results also imply that the order of the stiffness values of the surfaces examined, from high to low, is: (0001)  $V_2AlC$  > (0001)  $Cr_2AlC$  >  $(10\bar{1}0)$   $Cr_2AlC$  >  $SiO_2$ .

### B. Stiffness vs contact radius curves

When  $S$  is plotted vs  $a$  over the entire range, for the  $V_2AlC$  and  $Cr_2AlC$  (0001) and  $Cr_2AlC$   $(10\bar{1}0)$  indented surfaces, using the Berkovich [Fig. 2(a)] and  $5\ \mu m$  spherical tips [Fig. 2(b)], a linear relationship is obtained as expected from Eq. (A3). Herein we assume that the moduli obtained for the (0001) and  $(10\bar{1}0)$  crystal orientations are equal to  $c_{33}^{NI}$  and  $c_{11}^{NI}$ , respectively. The latter are listed in Table I. The reproducibility of the curves in the various locations is noteworthy.

Figure 2(c) plots typical values of the elastic constants as a function of total displacement  $h_t$ . After an initial relatively

large drop in moduli, the results plateau at  $h_t \approx 200$  nm. Unfortunately, for the MAX phases, the plateau is not level but slopes downward with increasing  $h_t$ . This renders determination of the true value of the elastic constants problematic. However, a perusal of the results shown in Figs. 2(a) and 2(b) indicates that past a contact radius of 750 nm, the results become noisier. It is for this reason that Table I reports the moduli at  $a = 750$  nm.

As noted above the Young's modulus of standard fused silica was obtained first, following the same aforementioned methods of measurement and calculation, for 12 different locations, to be  $76 \pm 1$  and  $68 \pm 1.5$  GPa for the Berkovich and  $5\ \mu m$  spherical indenter tips, respectively. It follows that both tips estimate the established modulus of 72 GPa [12], within a narrow range of 6%. In other words, in our setup, the Berkovich and spherical indenters are 6% higher and lower than the true value, correspondingly.

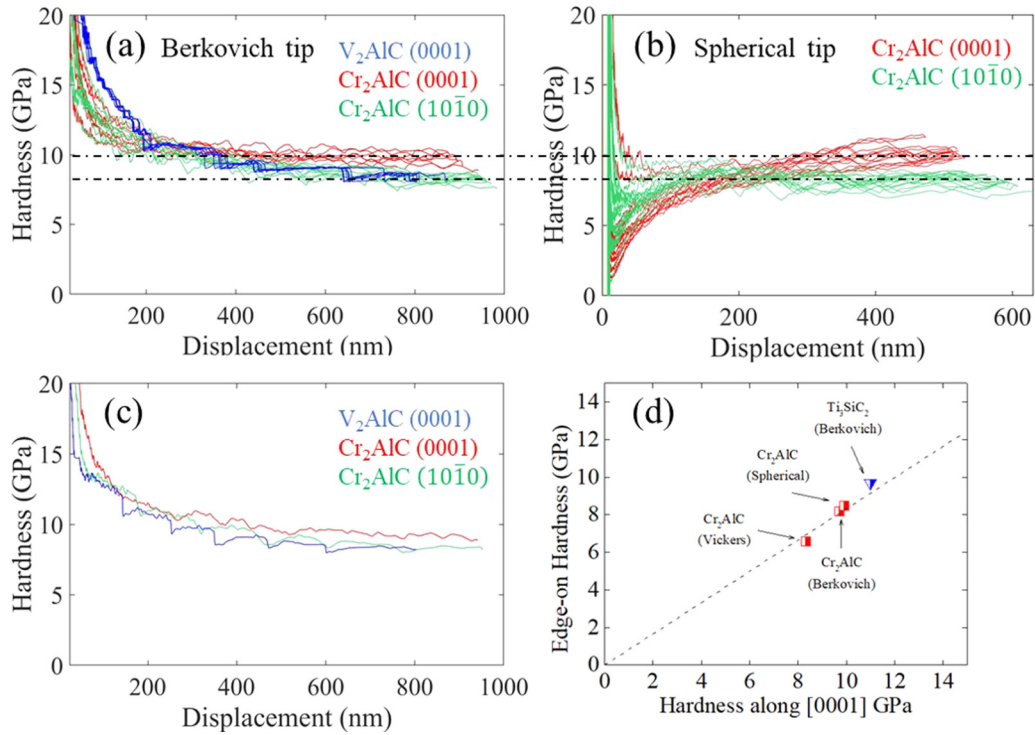


FIG. 4. Hardness vs displacement for V<sub>2</sub>AlC and Cr<sub>2</sub>AlC (0001) and Cr<sub>2</sub>AlC (10 $\bar{1}$ 0) surfaces obtained using (a) a Berkovich and (b) a 5  $\mu$ m-radius spherical indenter. (c) Same as (a) but with only three isolated curves, one per each system. (d) Hardness values obtained when loading Cr<sub>2</sub>AlC crystals along [0001] and edge-on with Berkovich, Vickers, and spherical indenters. Also plotted are the Berkovich results of Kooi *et al.* on Ti<sub>3</sub>SiC<sub>2</sub> [18].

**C. Stress vs strain curves**

When results such as the ones shown in Fig. 1(b) are converted to NI stress vs  $a/R$  plots (Fig. 3), the shapes of the curves and the information they relay are altered considerably. Typical results for the (0001) V<sub>2</sub>AlC surfaces are shown in Figs. 3(a) and 3(b). Those for the two Cr<sub>2</sub>AlC surfaces are plotted in Figs. 3(c)–3(f). These results reveal the following:

TABLE II. Summary of hardness values in GPa obtained herein and in previous work. The hardness values are obtained at a total indentation depth of 800 nm for the Berkovich and 500 nm for the spherical indenters. Numbers in parentheses denote the total number of indents performed to obtain the average and standard deviations reported.

Method	Orientation	V <sub>2</sub> AlC	Cr <sub>2</sub> AlC
		(GPa)	(GPa)
This work			
Berkovich	(0001)	8.8 $\pm$ 0.3 (19)	9.7 $\pm$ 0.3 (18)
Berkovich	(10 $\bar{1}$ 0)		8.4 $\pm$ 0.4 (28)
Vickers	(0001)	9.3 $\pm$ 0.8 (3)	8.3 $\pm$ 0.8 (3)
Vickers	(10 $\bar{1}$ 0)		6.6 $\pm$ 0.5 (3)
spherical	(0001)	7.8 $\pm$ 0.5 (3)	9.9 $\pm$ 0.4 (18)
spherical	(10 $\bar{1}$ 0)		8.5 $\pm$ 0.4 (28)
Previous work			
Berkovich	thin film	11.5 $\pm$ 1.7 [32]	13 $\pm$ 2 [33]
Vickers	polycrystal	1.9–2.9 [34]	3.5 [40]

(i) The response of the V<sub>2</sub>AlC (0001) surfaces [Fig. 3(a)] is stochastic in nature. In some locations large pop-ins were observed, while in others there were no pop-ins despite the fact that the applied stress was of the order of 20 GPa. In one location, the pop-in stress was 16 GPa [Fig. 3(b)]. When the applied load was reduced to 90 mN, rather than 120 mN,

TABLE III. Computed lattice parameters, elastic constants, and moduli in GPa of V<sub>2</sub>AlC and Cr<sub>2</sub>AlC single crystals. For the sake of comparison, we averaged previous theoretical results from Ref. [4].

Computed data	V <sub>2</sub> AlC (GPa)			Cr <sub>2</sub> AlC (GPa)		
	PBE <sup>a</sup>	PBE <sup>b</sup>	Literature <sup>c</sup>	PBE <sup>a</sup>	PBE <sup>b</sup>	Literature <sup>c</sup>
$a = b(\text{\AA})$	2.907	2.912	2.914	2.841	2.860	2.848
$c(\text{\AA})$	13.122	13.140	13.110	12.686	12.820	12.680
$V(\text{\AA}^3)$	96.041	96.469	96.408	88.699	90.814	89.070
$c_{11}$	332	328	341	369	347	359
$c_{12}$	77	74	78	87	77	75
$c_{13}$	105	102	118	108	91	99
$c_{33}$	326	320	320	360	332	389
$c_{44}$	152	150	151	143	129	138
$B_H$	174	170	186	189	172	204
$G_H$	132	131	133	138	130	139
$E_H$	316	312	319	333	311	333
$V$	0.20	0.19	0.2	0.21	0.20	0.21

<sup>a</sup>This work, relaxed cell.

<sup>b</sup>This work, but starting with experimental lattice parameters.

<sup>c</sup>Average of previous theoretical results listed in Ref. [4].

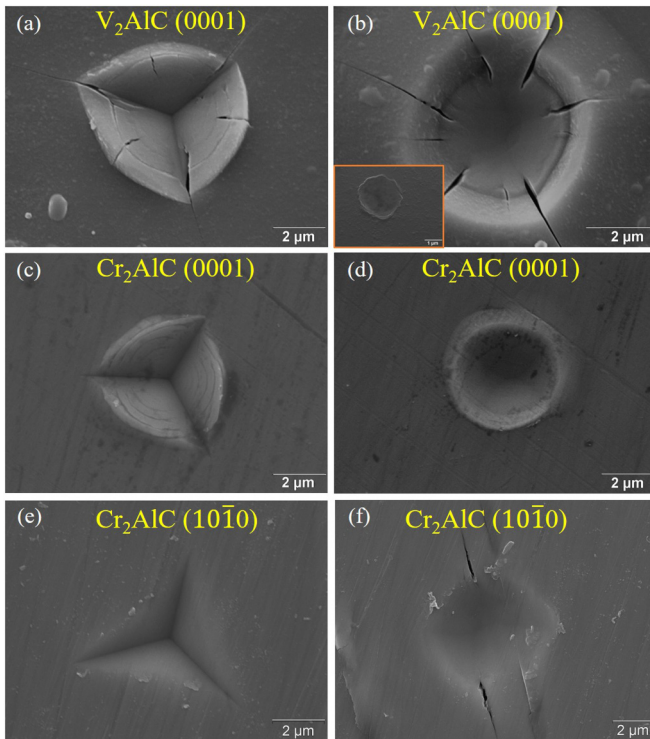


FIG. 5. Typical SEM micrographs of indentation marks made by a Berkovich (left column) and a  $5\ \mu\text{m}$  spherical tip (right column) on (a) and (b)  $\text{V}_2\text{AlC}$  (0001) surfaces. Inset shows the indentation mark observed when no pop-ins were registered. Also shown are plots on (c) and (d) (0001) and (e) and (f)  $(10\bar{1}0)$   $\text{Cr}_2\text{AlC}$  surfaces. The maximum load in (a) and (b) was 150 mN, (c) and (d), 100 mN, and (e) and (f) 120 mN.

pop-ins were only observed in 3 out of 14 locations as compared to 4 of 7 locations at the higher load.

(ii) Little deformation prior to the pop-in was observed. After the pop-ins, the maximum stresses that were sustained by the surfaces were of the order of 7 GPa [Fig. 3(a)]. As discussed below, this maximum stress is equated to the hardness.

(iii) The extent of the pop-ins also correlates to the pop-in stresses. When the pop-in stress was approximately 20 GPa, the pop-in extended to an  $a/R$  of 0.5 [Fig. 3(b)]. When the pop-in stress was 16 GPa, the extent of the pop-in was closer to 0.4 [Fig. 3(b)]. As importantly, in the absence of pop-ins, the indentation marks were considerably *smaller* in extent and depth [see inset in Fig. 5(b)].

(iv) The response of the  $(10\bar{1}0)$  and (0001)  $\text{Cr}_2\text{AlC}$  surfaces, shown in Figs. 3(c) and 3(d), respectively, were different in that the maximum sustained stresses were less than 20 GPa. The averages of the maximum stresses for the  $(10\bar{1}0)$  and (0001) surfaces were  $7.0 \pm 0.3$  and  $8.2 \pm 0.3$  GPa, respectively. The reproducibility between the various locations, for the most part, is also quite good.

(v) Figure 3(e) shows that for both  $\text{Cr}_2\text{AlC}$  surfaces an initial linear response is followed by a change in slope at a critical or microyielding stress, denoted by  $\sigma_c$ . The values of  $\sigma_c$  are  $3.0 \pm 0.3$  and  $2.4 \pm 0.2$  GPa, for the  $(10\bar{1}0)$  and (0001) surfaces, respectively.

(vi) The moduli obtained from the slopes of the linear parts of the stress vs  $a/R$  curves are significantly smaller than those obtained from the Berkovich tip.

Like other kinking nonlinear elastic (KNE) solids [39], fully, and spontaneously, reversible stress-strain hysteresis loops are obtained by cyclically indenting both  $\text{Cr}_2\text{AlC}$  surfaces. All 12 loops are shown in Fig. 3(f). The energy dissipated per unit volume per cycle  $W_d$  is significantly greater for the  $(10\bar{1}0)$   $\text{Cr}_2\text{AlC}$  surface than its (0001) counterpart. Furthermore, after the pop-ins, the (0001) surface is harder than its  $(10\bar{1}0)$  counterpart. At low loads, the former is less stiff however.

#### D. Hardness measurements

The Berkovich,  $H_{Br}$ , and Vickers hardness,  $H_V$ , results for all the crystal orientations tested are listed in Table II. Profiles of  $H_{Br}$  vs NI displacement are shown in Figs. 4(a) and 4(b). Note that the  $(10\bar{1}0)$   $\text{V}_2\text{AlC}$  surface was too narrow for us to measure its hardness. As noted above, the hardness values determined by the spherical indenter were taken to equal the average maximum stresses of the loops shown in Figs. 3(c) and 3(d) for the (0001) and  $(10\bar{1}0)$   $\text{Cr}_2\text{AlC}$  surfaces, respectively. For the  $\text{V}_2\text{AlC}$  (0001) surface, the hardness was taken as the average of the maxima of the cycles *after* the pop-ins shown in Fig. 3(a).

#### E. Scanning electron microscope micrographs

Typical postindentation SEM micrographs of the (0001)  $\text{V}_2\text{AlC}$ , (0001)  $\text{Cr}_2\text{AlC}$ , and  $(10\bar{1}0)$   $\text{Cr}_2\text{AlC}$  surfaces, using the Berkovich and spherical tips, are shown in Fig. 5. Those for the Vickers indentations are shown in Fig. 6. A perusal of these micrographs establishes the following. (i) For the (0001) surfaces [Figs. 5(a)–5(d), 6(a), and 6(c)] there is considerable pileup of material around the edges of the indentation marks. (ii) The shapes of the mounds, especially those created by the spherical indenter, is a function of composition. For the (0001)  $\text{Cr}_2\text{AlC}$  surfaces, the width of the rim is approximately  $1\ \mu\text{m}$  [Fig. 5(d)]. For the corresponding  $\text{V}_2\text{AlC}$  surface [Fig. 5(b)] the width of the rim is closer to  $5\ \mu\text{m}$ . In other words, the extent of deformation in the lateral direction is roughly 5 times higher for the (0001)  $\text{V}_2\text{AlC}$  surface compared to  $\text{Cr}_2\text{AlC}$ . (iii) Cracks appear on the  $\text{V}_2\text{AlC}$ , but not the  $\text{Cr}_2\text{AlC}$ , surfaces. (iv) For the  $(10\bar{1}0)$   $\text{Cr}_2\text{AlC}$  surfaces [Figs. 5(e), 5(f), and 6(b)] *no* pileup or mounding is observed at the edges of the indentation mark. Instead, delamination cracks are observed.

#### F. Computational results

Table III lists the lattice parameters and elastic constants and moduli, calculated herein. Also listed are the averages of the results found in the literature. For the most part, the agreement is satisfactory.

### V. DISCUSSION

#### A. Elastic moduli

For the most part, due to the presence of defects (see next section), the moduli obtained from the spherical indenter

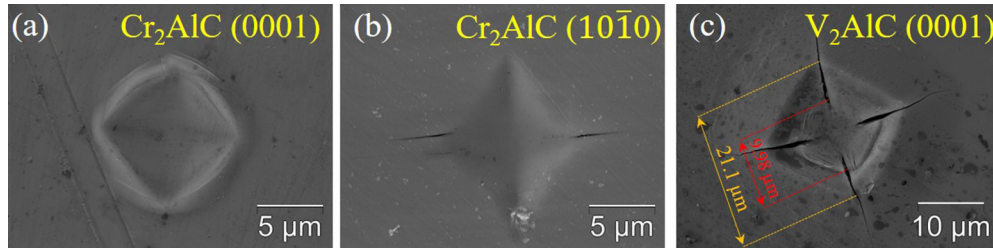


FIG. 6. Typical SEM micrographs of indentation marks made by a Vickers microindenter at a load of 0.49 N on (a)  $\text{Cr}_2\text{AlC}$  (0001), (b)  $\text{Cr}_2\text{AlC}$  ( $10\bar{1}0$ ), and (c)  $\text{V}_2\text{AlC}$  (0001) surfaces.

were lower; by an average of 25% and 30%, for the  $\text{Cr}_2\text{AlC}$  crystals than the ones obtained from the Berkovich tip or those calculated by DFT, respectively. Consequently, we will only compare the latter two. In that respect, the agreement has to be considered quite good, the largest difference being of the order of 15%. There are some important discrepancies, however, that need to be pointed out. For instance, theory predicts  $c_{11} > c_{33}$ , while experimentally we find the opposite. The reasons for this state of affairs are unclear at this time and more work is needed to reconcile the differences.

Importantly, all the  $c_{ij}$  values obtained herein are close to each other, which confirms once again that the MAX phases are elastically relatively isotropic especially compared to other known layered solids such as graphite and mica. For example,  $c_{33}$  and  $c_{11}$  of  $\text{Ti}_3\text{SiC}_2$  have been theoretically predicted [41] and experimentally measured [42] to be almost equal. When our results for  $\text{V}_2\text{AlC}$  are compared with previously reported experimental data of Young's moduli ( $E = 322$  GPa) by Sigumonrong *et al.* [32] and to a previously computed  $c_{33}$  values, 321 GPa on average [37,43], the agreement is good. The same is true for the  $\text{Cr}_2\text{AlC}$  surfaces (Table I) [33,35]. Overall, based on the entries in Table I, it is obvious that the measured and calculated elastic constants fall in the relatively narrow range of 317–347 GPa, with the DFT values being mostly on the higher side.

### B. Effect of defects

Previously, we have shown that when the pop-in stresses were high, of the order of  $c_{44}/n$ , where  $n < 10$ , as is the case herein for  $\text{V}_2\text{AlC}$  [Fig. 3(a)], this implied that our crystals were quite defect-free to begin with [45]. When the pop-in stresses are of the order of  $c_{44}/n$ , with  $n < 10$ , one is approaching a bond's theoretical limits. We [2] and others [44] have also previously shown that the distribution of pop-in stresses is stochastic in nature and can be described by Weibull statistics. The results for  $\text{V}_2\text{AlC}$  are fully consistent with this notion. The fact that the slopes of the linear regimes in Fig. 3(b) yield an elastic constant of  $290 \pm 14$  GPa, which is slightly lower than the value predicted by DFT, implies that our crystals were defect-free, at least at the volumes probed by the indenters. Interestingly, the moduli determined by the Berkovich tip are less sensitive to defects because of its shape.

We note in passing that the  $c_{44}/n$  where  $n < 10$  criterion for deformation of perfect crystals is shear based [45]. Here the failure criterion will most likely be buckling of the basal planes. It follows that an alternative buckling criterion needs to be developed. Nevertheless, the criterion in a perfect solid

will most likely be such that  $n$  will also be of the order of 10 or less.

The maximum load sustained by either of the  $\text{Cr}_2\text{AlC}$  surfaces, on the other hand, was at best half of those sustained by the  $\text{V}_2\text{AlC}$  surfaces. This strongly points to the fact that the  $\text{Cr}_2\text{AlC}$  crystals were significantly more defective. This conclusion is bolstered by the NI stress vs  $a/R$  plots for  $\text{Cr}_2\text{AlC}$  [Figs. 3(c) and 3(d)], where large pop-ins are notably absent. Instead, a large number of small pop-ins are observed.

Furthermore, when the initial slopes of the NI stress vs  $a/R$  plots are converted to elastic moduli the values obtained are significantly lower than the  $c_{ij}$  values listed in Table III. In the same way that microyielding, viz., the bowing of dislocation lines when some metals are loaded, results in moduli that are lower than those expected from, say, Young's moduli obtained from ultrasound measurements, the initial linear slopes shown in Figs. 3(e) and 3(f) are most probably due to the to-and-fro motion of *preexisting* ripplocations. In this case,  $\sigma_c$  coincides with the nucleation of new ripplocations in the presence of preexisting ones. Indenting thin steel sheets edge-on, we have shown that the nucleation stresses for BRs are greatly reduced when the latter are present [9]. In other words, ripplocations are potent nucleation sites for new ones.

It is the lack of such defects in the  $\text{V}_2\text{AlC}$  samples that allows them to sustain stresses up to 20 GPa [Fig. 3(a)]. After the pop-ins, the  $\sigma_c$  is of the order of 7 GPa [Fig. 3(b)]. Recall that  $\sigma_c$  is the stress needed to nucleate ripplocations in the presence of preexisting ones. For the  $\text{Cr}_2\text{AlC}$  surfaces,  $\sigma_c$  is of the order of 3 GPa and the presence of preexisting defects is what prevents the stresses to rise above the maximum values—equated to the hardness—shown in Figs. 3(c)–3(f).

### C. Fully and spontaneously reversible loops

Over the past few years, we made the case that the hallmarks of deformation by ripplocations and ripplocation boundaries are the large pileup of material around indentations edges when the basal planes are loaded along [0001] and delamination cracks when they are loaded edge-on as observed here (see Figs. 5 and 6). Another signature is the generation of fully reversible stress-strain curves when the same locations are repeatedly loaded. The generation of the latter is clear in Fig. 3(f) when the  $\text{Cr}_2\text{AlC}$  basal planes are loaded edge-on. When the load is applied along [0001], fully reversible loops are also observed, but  $W_d$  is smaller and the loops are stiffer [Fig. 3(f)]. In a ripplocation framework these differences can be understood as follows. When the basal planes are loaded edge-on, layer buckling is natural and

the entire applied load is used to buckle the layers. When the load is applied along [0001], on the other hand, the situation is different in that now only the projection of the applied stress normal to the indentation direction, i.e., along the basal planes, can result in buckling. That projected stress, by definition, has to be smaller than the applied one. Another possible reason for this state of affairs is the fact that after large pop-ins a new microstructure develops under the NI that is more polycrystalline in nature with quite small domains and multiple micro- and nanocracks [10]. The basal planes in the latter are less prone to buckle, which would also explain the stiffening of the loops and the lower values of  $W_d$ .

#### D. Hardness and its anisotropy

Figures 4(a) and 4(b) plot the NI hardness vs displacement profiles of the three surfaces explored herein obtained with the Berkovich and spherical indenters, respectively. The horizontal dashed lines indicate that both indenters yield comparable values. Based on these results, it is reasonable to conclude that the hardness of the  $\text{Cr}_2\text{AlC}$  (0001) surface is  $9.7 \pm 0.3$  GPa. Similarly, the hardness value of the  $\text{Cr}_2\text{AlC}$  ( $10\bar{1}0$ ) surface levels off at  $8.4 \pm 0.4$  GPa. These values are the ones reported in Table II. We note is passing that the agreement between the two sets of results is gratifying and is indirect evidence that our conversion of the load-displacement results to NI stresses vs  $a/R$  plots is reasonable and tethered to reality.

These values, however, have to be slightly tempered by the fact that if looked at individually, the hardness vs displacement profiles do not always reach a plateau. This is best seen in Fig. 4(c), where we isolated three hardness vs displacement curves, one for each of the surfaces tested. When so isolated, it is obvious that after an initial drop in hardness, the curves are not continuous but are stepped with small steps, each approximately 0.8 GPa [see Figs. 4(a) and 4(c)]. These steplike drops correspond to a cascade of pop-in events [Fig. 1(a)] and suggest that the nucleation of RBs and their motion is not continuous, but rather occurs in sudden successive drops. Obviously, such a response is fully consistent with successive buckling.

For the most part, loading the  $\text{V}_2\text{AlC}$  (0001) surface with the spherical tip showed no pop-ins during first loading, i.e., no plastic deformation. However, upon reloading the maximum sustainable stress was  $7.8 \pm 0.5$  GPa [Fig. 3(a)]. This value is slightly lower than the other hardness measurements listed in Table II, but is close enough that this maximum stress can be taken as a measure of hardness.

Figure 4(d) depicts the hardness values obtained at maximum indentation depths, using the Berkovich, spherical and Vickers indenters, on the (0001) and ( $10\bar{1}0$ )  $\text{Cr}_2\text{AlC}$  surfaces plotted on the  $x$  and  $y$  axes, respectively. The results of Kooi *et al.* [18], who measured the hardness anisotropy in  $\text{Ti}_3\text{SiC}_2$ , using a Berkovich tip, are also plotted. Note the hardness values of  $\text{Cr}_2\text{AlC}$  reported herein and those on  $\text{Ti}_3\text{SiC}_2$  are compared at the same indentation depth (approximately 800 nm). From these results it is reasonable to conclude that the hardness values of the (0001) and ( $10\bar{1}0$ ) surfaces, of at least  $\text{Cr}_2\text{AlC}$  and  $\text{Ti}_3\text{SiC}_2$ , are anisotropic, with the former being approximately 20% harder. Note the good agreement between the hardness values, measured on the

$\text{Cr}_2\text{AlC}$  surfaces, obtained using the Berkovich and spherical tips. Additionally, the Vickers microhardness value is roughly 80% lower than the NI ones. Since our  $\text{V}_2\text{AlC}$  samples were too thin to measure the hardness of their ( $10\bar{1}0$ ) surfaces, no conclusions concerning their anisotropy could be reached.

The hardness anisotropy can be related to the micromechanics of deformation of these materials. We have previously shown that the MAX phases deform, especially when the basal planes are loaded edge-on, or parallel to [0001] as done here, by the nucleation of, first, reversible RBs, which transform, at higher stresses, into irreversible KBs [10]. Consequently, we have shown that the stresses needed for the nucleation of RBs when the basal planes are loaded edge-on is significantly, up to a factor of 2, lower than when the load is applied along [0001] [10]. Note that in a basal dislocation framework, there should be little anisotropy since, in both orientations, the Schmidt factors are quite low and comparable.

Our results may also shed some light on the large discrepancy between hardness values measured on single crystals/grains vs those measured on polycrystalline samples that are usually significantly smaller. For example, consider a typical Vickers indentation mark on the ( $10\bar{1}0$ )  $\text{Cr}_2\text{AlC}$  crystal [Fig. 6(b)]: The [0001] diagonal is 30% larger than that parallel to the basal planes, which confirms once again the plastic anisotropy of the MAX phases. Turning to the corresponding Vickers indentation mark on the (0001)  $\text{V}_2\text{AlC}$  surface [Fig. 6(c)], if the lengths of the larger diagonals (approximately  $21 \mu\text{m}$ ) are used to calculate the hardness, a value of approximately  $2.1 \pm 0.2$  GPa is obtained, which coincidentally or not is in good agreement with the one reported by Hu *et al.* [34] on polycrystalline  $\text{V}_2\text{AlC}$  samples. However, this value is considerably lower than the value measured herein using the Berkovich tip, viz.,  $8.8 \pm 0.3$  GPa, on the same surface. If instead the smaller inner diagonal length ( $10 \mu\text{m}$ ) is used, the resulting hardness, at  $9.3 \pm 0.8$  GPa is considerably closer to the Berkovich hardness and thus more plausible. Hardness values of the same range obtained herein have been previously reported for  $\text{Cr}_2\text{AlC}$  [33] and  $\text{V}_2\text{AlC}$  [32] thin films. These results were explained on the basis of hardening promoted by the nanosize of the grains.

In the absence of large pop-ins, there is much less buildup of material near the indentation edges for the (0001)  $\text{V}_2\text{AlC}$  surface [see the inset of Fig. 5(b)]. There is thus little doubt that the pop-ins result in considerable material redistribution. One advantage of using spherical, rather than Berkovich, indenters in probing KNE behavior is that in the former case, considerable energy can be stored before the nucleation of the BRs. That excess energy is what results in the redistribution of material and/or delamination cracks. The higher the pop-in stresses, the higher the energy stored, which manifests itself in a larger postindentation penetration as clearly seen in Fig. 3(b). The Berkovich tip, on the other hand, severs the layers, which in turn results in much less elastic energy stored during the entire process. It is for this reason that the extent of pop-ins, if they occur at all, is significantly smaller when the Berkovich tip is used. This is also probably why the Berkovich tip is better at measuring the true elastic moduli of solids; there is less stored energy that can skew the results and the shape of the indents.

Finally, a comparison of the indents made in the (0001)  $V_2AlC$  [Fig. 6(c)] and  $Cr_2AlC$  [Fig. 6(a)] surfaces suggests that the latter is more ductile in that no cracks are nucleated. Another crucial difference is the extent of material pushed to the indent edges. In  $Cr_2AlC$ , a thin relatively narrow ring, where the difference between the inner and outer diameters is small, forms [see Figs. 5(d) and 6(a)]. In the  $V_2AlC$  case, the volcano-shape that forms extends over several micrometers.

## VI. CONCLUSION

Using microindentation/nanoindentation techniques, relatively large single crystals of  $V_2AlC$  and  $Cr_2AlC$  were used to estimate their elastic constants, hardness values, and shed light on their elastic-to-plastic transitions and KNE behavior. The values of  $c_{33}^{NI}$  and  $c_{11}^{NI}$ , determined using a Berkovich tip, at a contact radius of 750 nm, and those calculated by DFT, were all found to fall in the relatively narrow range of 320–350 GPa. It follows that the values of  $c_{11}$  and  $c_{33}$  are weak functions of chemistry and/or orientation, which confirms once more that the MAX phases are relatively elastically isotropic.

Similarly, the hardness values, obtained using Berkovich, 5  $\mu m$  spherical, and Vickers microindenters on the two  $Cr_2AlC$  surfaces were all comparable and fell in the narrow range of  $6.6 \pm 0.5$  to  $9.9 \pm 0.5$  GPa. In all cases, the (0001) surfaces were roughly 20% harder than when the basal planes were loaded edge-on, viz., the (10 $\bar{1}$ 0) surfaces. At  $9.9 \pm 0.4$  GPa, the hardness of the (0001)  $Cr_2AlC$  surface was the highest reported herein. The thinness of the  $V_2AlC$  samples did not allow us to measure any of their edge-on properties.

The (0001)  $V_2AlC$  surfaces were able to reproducibly sustain elastic stresses of the order of 20 GPa, which was not the case for either  $Cr_2AlC$  surface. It follows that the former were less defective than the latter. Roughly 60% of indentations, however, resulted in pop-ins, beyond which the maximum stresses sustainable drop to approximately 7 GPa. In some cases, the pop-ins were of the order of 300 nm and thus considerable. The pop-ins result in larger indentation marks wherein large pileups of material around the edges of the indentation marks resulted in volcano-shaped indentations similar to ones observed in mica [2] and graphite [1]. These pileups are absent in the absence of pop-ins. Repeated indentations in the same location after the pop-ins resulted in little energy dissipation.

Upon loading the (0001) and (10 $\bar{1}$ 0)  $Cr_2AlC$  surfaces, a number of small pop-ins (approximately 20 nm) were observed. The stresses at which these occur were all less than the maximum stresses sustained by these surfaces, viz.,  $8.2 \pm 0.3$  and  $7.0 \pm 0.2$  GPa, respectively. These values were comparable to the values obtained by the Berkovich and Vickers indenters on the same surfaces. Such good agreement between three quite differently shaped and sized tips is noteworthy and strongly suggests that our overall approach, and underlying assumptions, are solid and valid.

The results obtained here are also consistent with the nucleation and propagation of ripplocations and ripplocation boundaries. This is manifested by the aforementioned large buildup of material near the indentation mark edges [Figs. 5(a)–5(d), especially Figs. 5(b) and 5(d)] and the delamination cracks observed in Figs. 5(f) and 6(b). As we argued

several times, such cracks are irrefutable evidence for  $c$ -axis strain due to buckling [10].

Finally, the fact that  $W_d$  is higher for the (10 $\bar{1}$ 0)  $Cr_2AlC$  surfaces than the (0001) is also consistent with buckling for the simple reason that is easier to buckle layers if they are loaded edge-on than if they are loaded normal to them.

## ACKNOWLEDGMENTS

This work was funded by CMMI Division of NSF (Grant No. 1728041). M.W.B and T.O. were funded by a Chair-of-Excellence Program of the Nanosciences Foundation (Université Grenoble-Alpes Foundation). A.C. and J.-C.C. acknowledge financial support from the Fédération Wallonie-Bruxelles through the Action de Recherche Concertée on three-dimensional nanoarchitecturing of two-dimensional crystals (Grant No. 16/21-077), from the European Union's Horizon 2020 researchers and innovation program (Graphene Flagship Core 1, Program No. 696656, and Core 2, Program No. 785219), and from the Belgium FNRS. A.C. acknowledges support from Wallonie-Bruxelles-International. A.C. and J.-C.C are also indebted to the Flag-ERA JTC project entitled "MORE-MXenes." Computational resources were provided by the supercomputing facilities of the UCLouvain (CISM) and the Consortium des Equipements de Calcul Intensif en Fédération Wallonie-Bruxelles (CECI) funded by the Fonds de la Recherche Scientifique de Belgique (F.R.S.-FNRS) under convention No. 2.5020.11.

## APPENDIX: SPHERICAL NI DATA ANALYSIS

In a typical NI test, the load  $P$  and total displacement into the surface  $h_{tot}$  values were obtained. Additionally, harmonic contact stiffness  $S$  values were continuously provided, since the nanoindenter is equipped with a continuous stiffness measurement (CSM) option. The CSM technique measures  $S$  continually over the entire range of loading by superimposing a harmonic force on the nominally increasing load applied during NI [15]. The model followed here stands generally on the developments of the method first reported by Herbert *et al.* [46].

Figure 7 depicts the main parameters: total displacement  $h_t$ , contact depth  $h_c$ , contact radius  $a$ , and spherical tip radius  $R$ , required for nanoindentation data analysis. The contact

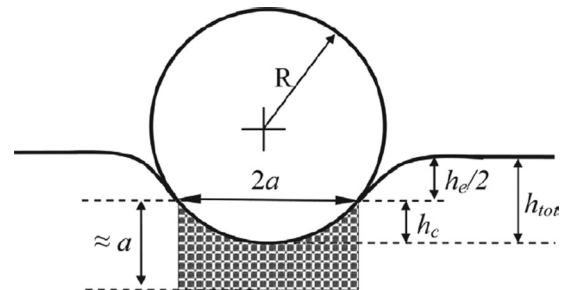


FIG. 7. Schematic of the spherical indenter and associated terms used in the text [12].

depth is first calculated assuming

$$h_c = h_t - \left( \frac{3P}{4S} \right). \quad (\text{A1})$$

Once  $h_c$  is obtained,  $a$  is calculated assuming

$$a = \sqrt{2Rh_c - h_c^2}. \quad (\text{A2})$$

Then, by assuming an isotropic elastic solid, indented by a spherical tip, the stiffness  $S$  is obtained by

$$S = 2E^*a, \quad (\text{A3})$$

where the reduced modulus  $E^*$  is determined from the slope of  $S$  vs  $a$  plots. Once  $E^*$  is determined, the sought after Young's

modulus  $E_s$  is calculated from

$$\frac{1}{E^*} = \frac{1 - \nu_s^2}{E_s} + \frac{1 - \nu_i^2}{E_i}, \quad (\text{A4})$$

where  $E_s$  and  $\nu_s$  are the specimen elastic modulus and its Poisson's ratio and  $E_i$  and  $\nu_i$  are the elastic modulus and Poisson's ratio of the diamond indenter assumed to be 1140 GPa and 0.07, respectively. Moreover, stress-strain plot can be derived by assuming NI stress  $\sigma_{\text{NI}} = \frac{P}{\pi a^2}$  and NI strain  $\epsilon_{\text{NI}} = \frac{a}{R}$  since in the elastic regime

$$\frac{P}{\pi a^2} = \frac{4}{3\pi} E^* \left( \frac{a}{R} \right). \quad (\text{A5})$$

Then the resulting slope of the linear elastic regime of the NI stress-strain curve is proportional to the reduced modulus  $E^*$ .

- 
- [1] M. W. Barsoum, A. Murugaiyah, S. R. Kalidindi, T. Zhen, and Y. Gogotsi, Kink bands, nonlinear elasticity and nanoindentations in graphite, *Carbon* **42**, 1435 (2004).
- [2] S. Basu, A. Zhou, and M. W. Barsoum, On spherical nanoindentations, kinking nonlinear elasticity of mica single crystals and their geological implications, *J. Struct. Geol.* **31**, 791 (2009).
- [3] M. Sokol, V. Natu, S. Kota, and M. W. Barsoum, On the chemical diversity of the MAX phases, *Trends Chem.* **1**, 210 (2019).
- [4] M. W. Barsoum, *MAX Phases: Properties of Machinable Ternary Carbides and Nitrides* (Wiley-VCH, Weinheim, 2013).
- [5] M. W. Barsoum, The  $M_{N+1}AX_N$  phases: A new class of solids; thermodynamically stable nanolaminates, *Prog. Solid State Chem.* **28**, 201 (2000).
- [6] M. W. Barsoum and M. Radovic, Elastic and mechanical properties of the MAX phases, *Annu. Rev. Mater. Res.* **41**, 195 (2011).
- [7] M. W. Barsoum and T. El-Raghy, Synthesis and characterization of a remarkable ceramic:  $\text{Ti}_3\text{SiC}_2$ , *J. Am. Ceram. Soc.* **79**, 1953 (1996).
- [8] M. W. Barsoum and G. J. Tucker, Deformation of layered solids: Ripplations not basal dislocations, *Scr. Mater.* **139**, 166 (2017).
- [9] M. W. Barsoum, Zhao, S. Shanazarov, A. Romanchuk, S. Koumlis, S. J. Pagano, L. Lamberson, and G. J. Tucker, Ripplations: A universal deformation mechanism in layered solids, *Phys. Rev. Mater.* **3**, 013602 (2019).
- [10] J. Griggs, A. C. Lang, J. Gruber, G. J. Tucker, M. L. Taheri, and M. W. Barsoum, Spherical nanoindentation, modeling and transmission electron microscopy evidence for ripplations in  $\text{Ti}_3\text{SiC}_2$ , *Acta Mater.* **131**, 141 (2017).
- [11] A. M. Johnson, *Styles of Folding: Mechanics And Mechanisms of Folding of Natural Elastic Materials* (Elsevier, Amsterdam, 1977).
- [12] S. Basu, A. Moseson, and M. W. Barsoum, On the determination of spherical nanoindentation stress-strain curves, *J. Mater. Res.* **21**, 2628 (2006).
- [13] O. Yeheskel, I. C. Albayrak, B. Anasori, and M. W. Barsoum, Mechanical and elastic properties of fine-grained polycrystalline scandia and erbia as determined by indentation techniques, *J. Eur. Ceram.* **31**, 1703 (2011).
- [14] I. C. Albayrak, S. Basu, A. Sakulich, O. Yeheskel, and M. W. Barsoum, Elastic and mechanical properties of polycrystalline transparent yttria as determined by indentation techniques, *J. Am. Ceram. Soc.* **93**, 2028 (2010).
- [15] W. C. Oliver and G. M. Pharr, An improved technique for determining hardness and elastic modulus using load and displacement sensing indentation experiments, *J. Mater. Res.* **7**, 1564 (1992).
- [16] T. Ouisse, E. Sarigiannidou, O. Chaix-Pluchery, H. Roussel, B. Doisneau, and D. Chaussende, High temperature solution growth and characterization of  $\text{Cr}_2\text{AlC}$  single crystals, *J. Cryst. Growth* **384**, 88 (2013).
- [17] L. Shi, T. Ouisse, E. Sarigiannidou, O. Chaix-Pluchery, H. Roussel, A. D. Chaussende, and B. Hackens, Synthesis of single crystals of  $\text{V}_2\text{AlC}$  phase by high-temperature solution growth and slow cooling technique, *Acta Mater.* **83**, 304 (2015).
- [18] B. J. Kooi, R. J. Poppen, N. J. M. Carvalho, J. T. M. De Hosson, M. W. Barsoum, and G. J. Tucker,  $\text{Ti}_3\text{SiC}_2$ : A damage tolerant ceramic studied with nanoindentations and transmission electron microscopy, *Acta Mater.* **51**, 2859 (2003).
- [19] P. Hohenberg and W. Kohn, Inhomogeneous electron gas, *Phys. Rev.* **136**, B864 (1964).
- [20] W. Kohn and L. J. Sham, Self-consistent equations including exchange and correlation effects, *Phys. Rev.* **140**, A1133 (1965).
- [21] G. Kresse and J. Hafner, *Ab initio* molecular dynamics for liquid metals, *Phys. Rev. B* **47**, 558 (1993).
- [22] G. Kresse and J. Furthmüller, Efficiency of ab-initio total energy calculations for metals and semiconductors using a plane-wave basis set, *Comput. Mater. Sci.* **6**, 15 (1996).
- [23] G. Kresse and J. Furthmüller, Efficient iterative schemes for *ab initio* total-energy calculations using a plane-wave basis set, *Phys. Rev. B* **54**, 11169 (1996).
- [24] J. Perdew, B. Kieron, and E. Matthias, Generalized Gradient Approximation Made Simple, *Phys. Rev. Lett.* **78**, 1396 (1996).

- [25] P. E. Blöchl, Projector augmented-wave method, *Phys. Rev. B* **50**, 17953 (1994).
- [26] G. Kresse and D. Joubert, From ultrasoft pseudopotentials to the projector augmented-wave method, *Phys. Rev. B* **59**, 1758 (1999).
- [27] J. Hendrik, Monkhorst, and J. D. Pack, Special points for Brillouin-zone integrations, *Phys. Rev. B* **13**, 5188 (1976).
- [28] A. Champagne, F. Bourdarot, P. Bourges, P. Piekarz, D. Pinek, I. Gélard, J.-C Charlier, and T. Ouisse, Phonon dispersion curves in Cr<sub>2</sub>AlC single-crystals, *Mater. Res. Lett.* **6**, 378 (2018).
- [29] W. Jeitschko, H. Nowotny, and F. Benesovsky, Kohlenstoffhaltige ternäre verbindungen (H-phase), *Monatsh. Chem.* **94**, 672 (1963).
- [30] Z. J. Wu, E.-J. Zhao, H.-P. Xiang, X.-F. Hao, X.-J. Liu, and J. Meng, Crystal structures and elastic properties of superhard IrN<sub>2</sub> and IrN<sub>3</sub> from first principles, *Phys. Rev. B* **76**, 054115 (2007).
- [31] R. Hill, The elastic behaviour of a crystalline aggregate, *Proc. Phys. Soc. London Ser. A* **65**, 349 (1952).
- [32] D. P. Sigumonrong, J. Zhang, Y. Zhou, D. Music, and J. M. Schneider, Synthesis and elastic properties of V<sub>2</sub>AlC thin films by magnetron sputtering from elemental targets, *J. Phys. D* **42**, 185408 (2009).
- [33] J. M. Schneider, D. P. Sigumonrong, D. Music, C. Walter, J. Emmerlich, R. Iskandar, and J. Mayer, Elastic properties of Cr<sub>2</sub>AlC thin films probed by nanoindentation and ab initio molecular dynamics, *Scr. Mater.* **57**, 1137 (2007).
- [34] C. Hu, L. He, M. Liu, X. Wang, J. Wang, M. Li, Y. Bao, and Y. Zhou, In situ reaction synthesis and mechanical properties of V<sub>2</sub>AlC, *J. Am. Ceram. Soc.* **91**, 4029 (2008).
- [35] J. D. Hettinger, S. E. Lofland, P. Finkel, T. Meehan, J. Palma, K. Harrell, S. Gupta, A. Ganguly, T. El-Raghy, and M. W. Barsoum, Electrical transport, thermal transport, and elastic properties of M<sub>2</sub>AlC (M = Ti, Cr, Nb, and V), *Phys. Rev. B* **72**, 115120 (2005).
- [36] M. F. Cover, O. Warschkow, M. M. M. Bilek, and D. R. McKenzie, A comprehensive survey of M<sub>2</sub>AX phase elastic properties, *J. Condens.: Matter Phys.* **21**, 305403 (2009).
- [37] Z. Sun, S. Li, R. Ahuja, and J. M. Schneider, Calculated elastic properties of M<sub>2</sub>AlC (M = Ti, V, Cr, Nb, and Ta), *Solid State Commun.* **129**, 589 (2004).
- [38] G. Jia and L. Yang, *Ab initio* calculations for properties of Ti<sub>2</sub>AlN and Cr<sub>2</sub>AlC, *Physica B* **405**, 4561 (2010).
- [39] M. W. Barsoum, A. Murugaiah, S. R. Kalidindi, and T. Zhen, Kinking Nonlinear Elastic Solids, Nanoindentations, and Geology, *Phys. Rev. Lett.* **92**, 255508 (2004).
- [40] W. Tian, P. Wang, G. Zhang, Y. Kan, Y. Li, and D. Yan, Synthesis and thermal and electrical properties of bulk Cr<sub>2</sub>AlC, *Scr. Mater.* **54**, 841 (2006).
- [41] B. Holm, R. Ahuja, and B. Johansson, *Ab initio* calculations of the mechanical properties of Ti<sub>3</sub>SiC<sub>2</sub>, *Appl. Phys. Lett.* **79**, 1450 (2001).
- [42] A. Murugaiah, M. W. Barsoum, S. R. Kalidindi, and T. Zhen, Spherical nanoindentations and kink bands in Ti<sub>3</sub>SiC<sub>2</sub>, *J. Mater. Res.* **19**, 1139 (2004).
- [43] J. Wang and Y. Zhou, Dependence of elastic stiffness on electronic band structure of nanolaminate M<sub>2</sub>AlC (M = Ti, V, Nb, and Cr) ceramics, *Phys. Rev. B* **69**, 214111 (2004).
- [44] J. Morris, H. Bei, G. M. Pharr, and E. P. George, Size Effects and Stochastic Behavior of Nanoindentation Pop In, *Phys. Rev. Lett.* **106**, 165502 (2011).
- [45] M. W. Barsoum, T. Zhen, A. Zhou, S. Basu, and S. R. Kalidindi, Microscale modeling of kinking nonlinear elastic solids, *Phys. Rev. B* **71**, 134101 (2005).
- [46] E. G. Herbert, G. M. Pharr, W. C. Oliver, B. N. Lucas, and J. L. Hayd, On the measurement of stress-strain curves by spherical indentation, *Thin Solid Films* **398-399**, 331 (2001).